THE JOURNAL OF IMMUNOLOGY

SARS-Coronavirus Open Reading Frame-9b Suppresses Innate Immunity by Targeting Mitochondria and the MAVS/TRAF3/TRAF6 Signalosome

Chong-Shan Shi, Hai-Yan Qi, Cedric Boularan, Ning-Na Huang, Mones Abu-Asab, James H. Shelhamer and John H. Kehrl

J Immunol published online 18 August 2014
http://www.jimmunol.org/content/early/2014/08/18/jimmunol.1303196

The Journal of Immunology is published twice each month by
The American Association of Immunologists, Inc.,
9650 Rockville Pike, Bethesda, MD 20814-3994.

Print ISSN: 0022-1767 Online ISSN: 1550-6606.

Published August 18, 2014, doi:10.4049/jimmunol.1303196

SARS-Coronavirus Open Reading Frame-9b Suppresses Innate Immunity by Targeting Mitochondria and the MAVS/TRAF3/TRAF6 Signalosome

Chong-Shan Shi,* Hai-Yan Qi,† Cedric Boularan,* Ning-Na Huang,* Mones Abu-Asab,‡ James H. Shelhamer,† and John H. Kehrl*

Coronaviruses (CoV) have recently emerged as potentially serious pathogens that can cause significant human morbidity and death. The severe acute respiratory syndrome (SARS)-CoV was identified as the etiologic agent of the 2002–2003 international SARS outbreak. Yet, how SARS evades innate immune responses to cause human disease remains poorly understood. In this study, we show that a protein encoded by SARS-CoV designated as open reading frame-9b (ORF-9b) localizes to mitochondria and causes mitochondrial elongation by triggering ubiquitination and proteasomal degradation of dynamin-like protein 1, a host protein involved in mitochondrial fission. Also, acting on mitochondria, ORF-9b targets the mitochondrial-associated adaptor molecule MAVS signalosome by usurping PCBP2 and the HECT domain E3 ligase AIP4 to trigger the degradation of MAVS, TRAF3, and TRAF 6. This severely limits host cell IFN responses. Reducing either PCBP2 or AIP4 expression substantially reversed the ORF-9b–mediated reduction of MAVS and the suppression of antiviral transcriptional responses. Finally, transient ORF-9b expression led to a strong induction of autophagy in cells. The induction of autophagy depended upon ATG5, a critical autophagy regulator, but the inhibition of MAVS signaling did not. These results indicate that SARS-CoV ORF-9b manipulates host cell mitochondria and mitochondrial function to help evade host innate immunity. This study has uncovered an important clue to the pathogenesis of SARS-CoV infection and illustrates the havoc that a small ORF can cause in cells. ***The Journal of Immunology*****, 2014, 193: 000–000.**

Severe acute respiratory syndrome (SARS) is caused by a novel coronavirus (SARS-CoV) (1–3). An international outbreak of SARS began in November 2002 and ended in July 2003. It afflicted >8000 people and left 774 patients dead (4, 5). Prior to the 2003 SARS outbreak, CoV had not been recognized as a significant pathogen. However, the subsequent documentation of a large pool of CoV that circulate in bats and other animals has portended the possible emergence of other highly pathogenic CoV as major threats to human health (6, 7). And recently, a SARS-like virus designated human corona virus-Eramus Medical Center or Middle East respiratory syndrome CoV has been detected in patients, whose clinical courses have resembled that of SARS patients, although with an even higher mortality rate (8, 9).

Shortly after the initial SARS outbreak, the genome sequence and organization of SARS-CoV were reported (10, 11). It is a large single-positive–strand RNA virus. The virus genome encodes eight accessory proteins designated open reading frame (ORF)-3a, 3b, 6, 7a, 7b, 8a, 8b, and 9b. Several have identified functions. ORF-3a triggers cellular apoptosis; ORF-7a activates NF-κB; ORF3b upregulates the expression of several cytokines and chemokines; ORF-6 reduces IFN production; ORF-8a triggers cellular apoptosis; and ORF-8b induces cellular DNA synthesis (12). However, the function of ORF-9b is largely unknown. Synthesized from an alternative complete reading frame within the viral N gene, the 98-aa protein has no known homolog. A resolved crystal structure revealed a dimeric tentlike β structure with an amphipathic surface and a central hydrophobic cavity that most likely mediates membrane attachment (13). The protein has been detected in tissues from infected patients and in in vitro infected cells (14, 15). Two previous studies have addressed the localization of ORF-9b in Vero cells, a cell line derived from African green monkey kidney epithelial cells (16, 17). In the first study, it was reported to be exported from the nucleus and to colocalize with an endoplasmic reticulum marker (16) and in a more recent study to shuttle between the nucleus and the cytosol via an interaction with Crm1 (17).

SARS-CoV–infected cells have an impaired IFN response, suggesting that the virus disrupts the normal host cell IFN response (18). Yet, IFN therapy has also been suggested to be efficacious for SARS patients (18, 19). The activation of the type 1 IFN pathway is crucial for the control of many viral infections. Following viral invasion, host cells detect the presence of viral RNA by endosomally localized TLR and cytosolic sensors of the retinoic-inducible gene-I (RIG-I)–like receptor (RLR) pathway, RIG-I and melanoma differentiation-associated gene 5 (MDA5) (20). RIG-I and MDA5 consist of two N-terminal CARDs, a central

*B Cell Molecular Immunology Section, Laboratory of Immunoregulation, National Institute of Allergy and Infectious Diseases, National Institutes of Health, Bethesda, MD 20892; †Critical Care Medicine Department, National Institutes of Health, Bethesda, MD 20892; and ‡Immunopathology Section, National Eye Institute, National Institutes of Health, Bethesda, MD 20892

Received for publication November 27, 2013. Accepted for publication July 19, 2014.

This work was supported by the Intramural Research Program of the National Institutes of Health (National Institute of Allergy and Infectious Diseases).

Address correspondence and reprint requests to Dr. John H. Kehrl, Laboratory of Immunoregulation, National Institute of Allergy and Infectious Diseases, National Institutes of Health, Building 10, Room 11B08, 10 Center Drive, MSC 1876, Bethesda, MD 20892. E-mail address: jkehrl@niaid.nih.gov

The online version of this article contains supplemental material.

Abbreviations used in this article: CoV, coronavirus; DRP1, dynamin-like protein 1; IRF, IFN regulatory factor; MDA5, melanoma differentiation-associated gene 5; ORF, open reading frame; poly(I:C), polyinosinic-polycytidylic acid; RFP, red fluorescent protein; RIG-I, retinoic-inducible gene-I; RLR, RIG-I–like receptor; SARS, severe acute respiratory syndrome; shRNA, short hairpin RNA; siRNA, small interfering RNA; STED, stimulated emission depletion.

DEAD box helicase/ATPase domain and a C-terminal regulatory domain. Although RIG-I and MDA5 differ in the types of viral RNA that they recognize, they share a common signaling pathway that utilizes the adaptor protein, mitochondrial antiviral signaling protein MAVS (also known as ISP-1/VISA/Cardiff). The N-terminal MAVS CARD domain mediates the interaction with RIG-I and MDA5 as well with downstream effectors; an adjacent proline-rich region also recruits downstream signaling molecules; and the C-terminal transmembrane domain anchors the protein to the mitochondrial membrane. MAVS recruits the E3 ligases TRAF3 and TRAF6, facilitating the activation of IFN regulatory factors (IRFs), NF-κB, and the induction of a host antiviral state.

However, RNA viruses have evolved strategies to antagonize the type I IFN signaling pathways. MAVS and MAVS signaling are common targets. For example, the human metapneumovirus M2-2 protein inhibits cellular immunity by inhibiting MAVS signaling. The M2-2 protein interacted with MAVS; however, the specific mechanisms by which M2-2 functioned was not discerned (21). Enterovirus 71 employs a protease 2Apro to cleave and release MAVS from mitochondria, thereby deactivating the pathway and promoting viral immune evasion (22). Hepatitis C utilizes a similar mechanism as the viral protease NS3/4A also cleaves MAVS efficiently degrading mitochondria-associated membrane-associated MAVS (23, 24). The mitochondria-associated membrane is a specialized membrane subcompartment that links mitochondria to the endoplasmic reticulum–peroxisome network. The hepatitis B X protein also causes the degradation of MAVS by triggering its ubiquitination on Lys^{136} (25). Finally, respiratory syncytial virus uses two structural proteins, NS1 and NS2, to assemble a degradasome that also preferentially targets MAVS signaling (26). How SARS-CoV subverts the host IFN response is poorly understood.

In this study, we investigate the functional role of ORF-9b in cells and find that ORF-9b alters host cell mitochondria morphology and disrupts mitochondria antiviral signaling. ORF-9b localizes to the outer mitochondria membrane. Probably as a consequence, mitochondria elongate and mitochondrial antiviral signaling is disturbed. Furthermore, either as a direct or indirect consequence, autophagosome formation in acutely ORF-9b–expressing cells is enhanced.

Materials and Methods

Reagents and Abs

Hoechst 33342 (Invitrogen) was used at a concentration of 100 ng/ml. MG-132 (Cayman Chemical) was used at 10 μM, and 3 methyladenine (Sigma-Aldrich) at 5 nM. Primary Abs used for immunofluorescence experiments were the following: anti-MAVS (Cell Signaling; 1:500), anti-Flag (Sigma-Aldrich; 1:500), anti-Tomm20 (Santa Cruz Biotechnology; 1:1,000), and anti–dynamin-like protein 1 (DRP1) (BD Biosciences; 1:200). The secondary Abs used for immunofluorescence were as follows: polyclonal anti-mouse Ig Alexa488 or Alexa568 conjugated (Invitrogen; 1:1000); polyclonal anti-rabbit Ig Alexa488, Alexa568, or Alexa647 conjugated (Invitrogen; 1:1000); polyclonal goat anti-rabbit Ig ATTO647N (Active Motif; 1:1000); and polyclonal goat anti-mouse IgG MegaRed 520 (Sigma-Aldrich; 1:100). Primary Abs used for immunoblotting were the following: rabbit anti-MAVS, ATG5 and DRP1, mouse anti-GFP, and IFN-α (Cell Signaling); mouse anti-PCPB2 and anti-AIP4 (Santa Cruz Biotechnology); monoclonal anti-Myc (Clontech Laboratories); mouse anti-Flag and rabbit anti-LC3 (Sigma-Aldrich); rabbit anti-K48–linked polyubiquitin chains (Millipore); mouse monoclonal anti–IFN-β (BioLegend); and mouse anti-actin conjugated to HRP (Sigma-Aldrich). For immunoprecipitations, monoclonal mouse anti-Myc, anti-PCPB2 or anti-GFP, and protein G PLUS–agarose (Santa Cruz Biotechnology) were used.

Cells and plasmids

A549 and HEK 293 cells were obtained from the American Type Culture Collection. A549 and HEK 293 cells were maintained in DMEM supplemented with 10% FBS (Invitrogen). The A549 Tet-inducible 9b-GFP cells were made by transfecting A549 cells with pTet-on (Clontech), followed by G418 selection for 4 wk. Single clones were picked, expanded, and transfected with pTRE2 pur-9b-GFP (Clontech vector). These cells were selected with G418 and puromycin for 4 wk, after which the cell lines were treated with tetracycline and GFP-positive cells were sorted and allowed to re-expand in the absence of tetracycline. Low-frequency constitutively expressing 9b-GFP cells were also sorted and expanded. THP-1 cells expressing GFP or 9b-GFP were made transfecting the cells with the appropriate construct and selecting cells for 4 wk with G418. The top 5% of GFP-positive cells were sorted after 4 and 6 wk of selection. The cell lines were maintained in G418.

Atg5 and control small interfering RNA (siRNA) were purchased from Santa Cruz Biotechnology (Santa Cruz, CA). The LC3-GFP plasmid was a gift ofDr. Noboru Mizushima (Tokyo Metropolitan Institute of Medical Science, Tokyo, Japan), in which GFP was replaced by red fluorescent protein (RFP) as the autophagosome probe. Myc-MAVS full-length and its truncated constructs and full-length RIG-I and RIG-$I^{1–250}$ were gifts of Dr. Takumi Kushiba (Kyushu University, Fukuoka, Japan). Myc-MAVS (503–540) and Flag-Traf3 were gift of Dr. John Hiscott (Lady Davis Institute, Quebec, Canada). Mito-Cherry Red was a gift of Dr. Quan Chen (Chinese Academy of Sciences, Beijing, China). The IFN-β luciferase reporter was a gift ofDr. Saori Suzuki (University of Tokyo, Tokyo, Japan). The NF-κB luciferase reporter was provided by Dr. Ulrich Siebenlist (National Institutes of Health). SARS-CoV accessory ORF-9b DNA was generated by PCR from K14 and J17 cDNA clones, which were produced from the SARS-CoV genome Tor2 isolate (Michael Smith Genome Sciences Centre, Vancouver, Canada). The PCR primers were corresponding to SARS-CoV accessory gene sequences in accession number NC_004718 (http://www.ncbi.nlm.nih.gov/gene/).

Recombinant GFP-tagged SARS-CoV ORF-9b was generated using pEGFP-N1 vector (BD Biosciences). The ORF-9b constructs were verified by DNA sequencing. The plasmids were transiently transfected into the cells using Lipofectamine 2000 (Invitrogen) following the manufacturer's protocol.

Luciferase assay

HEK 293 cells (2×10^5 cells/well) were seeded in 24-well plates. The following day, the cells were cotransfected with 25 ng luciferase reporter plasmid, 2.5 ng *Renilla* luciferase internal control vector phRL-TK (Promega), and each of the indicated plasmids with Lipofectamine 2000 (Invitrogen). Empty vector pcDNA3 was used to maintain equivalent amounts of DNA in each well. The transfection of polyinosinic-polycytidylic acid [poly(I:C)] was performed 6 h before cell harvest. The reporter gene assay was performed 24 h after transfection and analyzed by a dual-luciferase reporter assay on the Mithras LB 840 Multimode Microplate Reader (Berthold). Each experiment was replicated a minimum of three times.

RNA-mediated interference

The siRNA pools targeting human ATG5 (sc-41445) or control siRNA (sc-37007) with scrambled sequence were purchased (Santa Cruz Biotechnology). The short hairpin RNAs (shRNAs) against human PCPB2 and AIP4 were designed on published targeting sequences (27). The synthetic DNA oligomers targeting PCPB2, AIP4, or scrambled sequence control were cloned into the pSIREN-RetroQ vector (Clontech). The DRP1 shRNA was a gift of Dr. Shigehisa Hirose (Tokyo Institute of Technology, Tokyo, Japan). For the knockdowns in A549 cells, the cells seeded for 4 h were transfected with siRNAs targeting ATG5 or control siRNA 30 nM once, and, on the following day, 10 nM siRNA was transfected again 8 h prior to harvesting the cells. The shRNAs were transfected into HEK 293 cells overnight, and then the cells were lysed for analysis. The transfections were performed using Lipofectamine 2000 (Invitrogen).

GFP-LC3 assay

These assays were done as described previously (28). A minimum of 50–100 GFP^+ cells per sample was surveyed, and the number of GFP-$LC3^+$ dots/cell was counted. Cells were considered positive if they had more than three large GFP-$LC3^+$ dots. Data are presented as a percentage of the total number of GFP^+ cells visualized.

Immunoblot analysis and immunoprecipitation

For standard immunoblotting, the cells were lysed in a buffer of 20 mM HEPES (pH 7.4), 50 mM β-glycerophosphate, 1 mM Na_3VO_4, 0.5% (v/v) Triton X-100, 0.5% (v/v) CHAPS, and 10% (v/v) glycerol with a protease inhibitor mixture tablet. For the LC3 immunoblot analysis, the cells were

lysed with the same buffer plus 0.25% SDS. The lysates were separated by SDS-PAGE and transferred to nitrocellulose membrane by iBLOT Gel Transfer System (Invitrogen). The membrane was incubated with 5% nonfat milk w/v in TBS buffer (25 mM Tris-HCl [pH 7.5], 150 mM NaCl, 0.1% Tween 20) for 1 h, and then reacted with the primary Ab in TBS buffer with 2.5% nonfat milk or 5% BSA w/v for overnight by shaking at 4˚C. The appropriated second Abs conjugated to HRP were used to detect the protein of interest via ECL. To immunoprecipitate Myc-MAVS or ORF8b-GFP, the cells were lysed in the same buffer and incubated for 2 h at 4˚C with the appropriate Abs, at which point protein G PLUS–agarose was added, followed by an additional incubation of 1 h at 4˚C. The immunoprecipitates were collected and washed eight times with lysis buffer, separated by SDS-PAGE, and analyzed by immunoblotting. To immunoprecipitate PCPB2, 1% CHAPS was used in the above buffer. To analyze ubiquitination, 2% SDS was added to the lysates prior to heating them to 95˚C for 10 min. Subsequently, the cell lysates were diluted 10-fold with the extraction buffer and then incubated with Abs overnight. Membranes were stripped using OneMinutePlus (GM Bioscience) following the manufacturer's protocol. Blots were scanned and imported into Photoshop as unmodified tagged image file format files. Quantification of band intensity was done using Photoshop.

Immunofluorescence

A549 cells were grown on 35-mm plates (MatTek) for confocal microscopy or on 0.15-mm coverslips (Corning) for stimulated emission depletion (STED) imaging, after which the cells were fixed in methanol for 5 min. After blocking for 1 h in 5% BSA in PBS–0.05% Tween 20, the cells were incubated for 1 h with the appropriated primary Ab at 4˚C, washed three times in PBS, and incubated with appropriate secondary Abs for 30 min at 4˚C. Hoescht33342 was applied for the last 5 min only for confocal experiments. After an extensive wash in PBS, cells were mounted in Prolong antifade reagent (Invitrogen) and were imaged on a Leica DMIRBE inverted microscope equipped with a TCS SP5 confocal scanner and a 63× 1.32 NA (Numerical Aperture) objective (Leica Microsystems).

High-resolution light microscopy

For STED microscopy and the corresponding confocal microscopy, a LEICA SP5-STED microscope was used. The fluorophores ATTO647N (Active Motif) and MegaRed (Sigma-Aldrich) were excited with an 80 MHz pulsed diode laser at 635 or 531 nm, respectively (Pico-Quant; pulse width <100 ps). STED depletion was achieved using a mode-locked titanium sapphire laser (Spectra Physics Mai Tai HP laser) operating at 770 nm with a repetition rate of 80 MHz. The delay between the excitation and STED pulses was adjusted electronically to optimize depletion. The excitation and the STED beams were focused by a 100× oil immersion objective (NA 1.4 PL APO STED, 100×; Leica Microsystems). The fluorescence signal was collected by the same objective and detected confocally between 650 and 690 nm for ATTO647N and between 540 and 595 nm for Megared with an APD detector. Using this setup, a resolution of ~250 nm in the confocal images and 50–70 nm in the STED images was achieved. Except for contrast stretching and level adjustment, no further image processing was applied.

Electron microscopy

For standard electron microscopy, HEK 293 cells were transfected with a control vector or 9b-Flag. The following day, the cells were double fixed in PBS-buffered glutaraldehyde (2.5%) and osmium tetroxide (0.5%), dehydrated, and embedded with Spurr's epoxy resin. Ultrathin sections (90 nm) were made and double stained with uranyl acetate and lead citrate and viewed in a JEOL JEM-1010 transmission electron microscope. For immunoelectron microscopy, HEK 293 cells were transfected with a control vector or 9b-Flag. The following day, the cells were fixed in formaldehyde, pelleted in 1.5% low melting point agarose, washed with PBS (3×, 5 min), dehydrated in an ethanol series, and embedded in LR White (SPI). Ultrathin sections were mounted on 150-mesh uncoated nickel grids. Grids were floated on blocking solution (PBS, 0.1% Tween 20, 0.5% cold-water fish gelatin [Ted Pella]) for 20 min, incubated for 1 h with the primary Abs, rinsed in blocking buffer for 5 min, blocked with 2% goat serum, rinsed with blocking buffer, and then incubated with 10 and 20 nm gold-conjugated secondary goat Ab accordingly (Ted Pella), rinsed in PBS, and air dried. Sections were stained with aqueous uranyl acetate (5%) and examined with a JEOL JEM-1010 electron microscope.

Flow cytometry

A549 cells stably expressing 9b-GFP or GFP were harvested and fixed with 4% paraformaldehyde for 20 min. After three washes in PBS 1% BSA, the cells were permeablized with ice-cold methanol for 5 min. After blocking for 1 h in PBS 1% BSA, the primary Ab (DRP1) was incubated for 3 h and secondary Alexa647-conjugated Ab was incubated for 40 min. Data were acquired with a FACS CANTO (BD Biosciences) and analyzed using FlowJo software.

Statistical analysis

Prism (GraphPad software) was used for all statistical analyses. All experiments were repeated a minimum of three times.

Results

SARS-CoV ORF-9b localizes to mitochondria and results in reduced DRP1 levels and mitochondrial elongation

Although SARS-CoV infects multiple organs, the pulmonary epithelium and immune cells are major targets (29, 30). To investigate the functions of ORF-9b, we first expressed an ORF-9b GFP fusion protein (9b-GFP) in A549 cells, a cell line used as a model of type II pulmonary epithelial cells. We found that ORF-9b localized to mitochondria and that those cells that expressed the fusion protein had more elongated mitochondria compared with control cells (Fig. 1A, 1B, Supplemental Video 1). Similar results were found following expression of 9b-GFP in HEK 293 cells (Fig. 1A). We also verified the mitochondrial morphology changes in a permanent transfection model using THP-1 cells, a human monocyte-like cell line that can be differentiated to macrophages following treatment with PMA. Immunostaining 9b-GFP–expressing THP-1 cells for the mitochondrial protein Tomm20 revealed numerous elongated mitochondria that colocalized with 9b-GFP (Fig. 1C). Mitochondrial fusion and fission maintain mitochondrial number, morphology, and function. In the initial step of fission, the dynamin-related protein DRP1 is recruited to mitochondria, where it assembles into a fission complex (31). As reduction in DRP1 favors mitochondrial fusion, we checked whether ORF-9b affected DRP1 levels. Expression of 9b-GFP in HEK 293 cells reduced DRP1 levels by ~70% via a mechanism sensitive to proteasome inhibition, but not autophagic degradation inhibition (Fig. 1D). We found similar results when we used a 9b-Flag construct (Fig. 1E). The sensitivity to proteasome inhibition suggested that DRP1 underwent ubiquitination. Consistent with that possibility, the immunoblotting of DRP1 immunoprecipitates revealed the presence of K48-linked ubiquitin (Fig. 1F). We also examined DRP1 levels in the permanently transfected THP-1 cells and again found a marked decrease in DRP1 levels (Fig. 1G). Further imaging and flow cytometry studies confirmed the reduction of DRP1 in 9b-GFP–expressing cells (Fig. 2A, 2B). The imaging data showed that some DRP1 is recruited to the 9b-GFP–delineated mitochondria. As transfection of 9b-GFP into A549 cells led to varying levels of 9b-GFP expression in individual cells, we checked the endogenous DRP1 expression in cells as a function of 9b-GFP levels (Fig. 2A). We found that those cells with higher levels of 9b-GFP had lower amounts of DRP1 and less DRP1 associated with mitochondria. Consistent with the presence of DRP1 and ORF-9b in the same molecular complex, endogenous DRP1 immunoprecipitates contained small amounts of 9b-GFP, but not GFP (Fig. 2C). These data show that ORF-9b localizes to mitochondria and most likely causes mitochondrial elongation by triggering DRP1 ubiquitination and its proteasomal destruction.

SARS-CoV ORF-9b limits host cell IFN signaling and coimmunoprecipitates with the mitochondrial adaptor protein MAVS

Besides their recognized role in energy production, mitochondria serve as a platform for host defense against RNA viruses such as

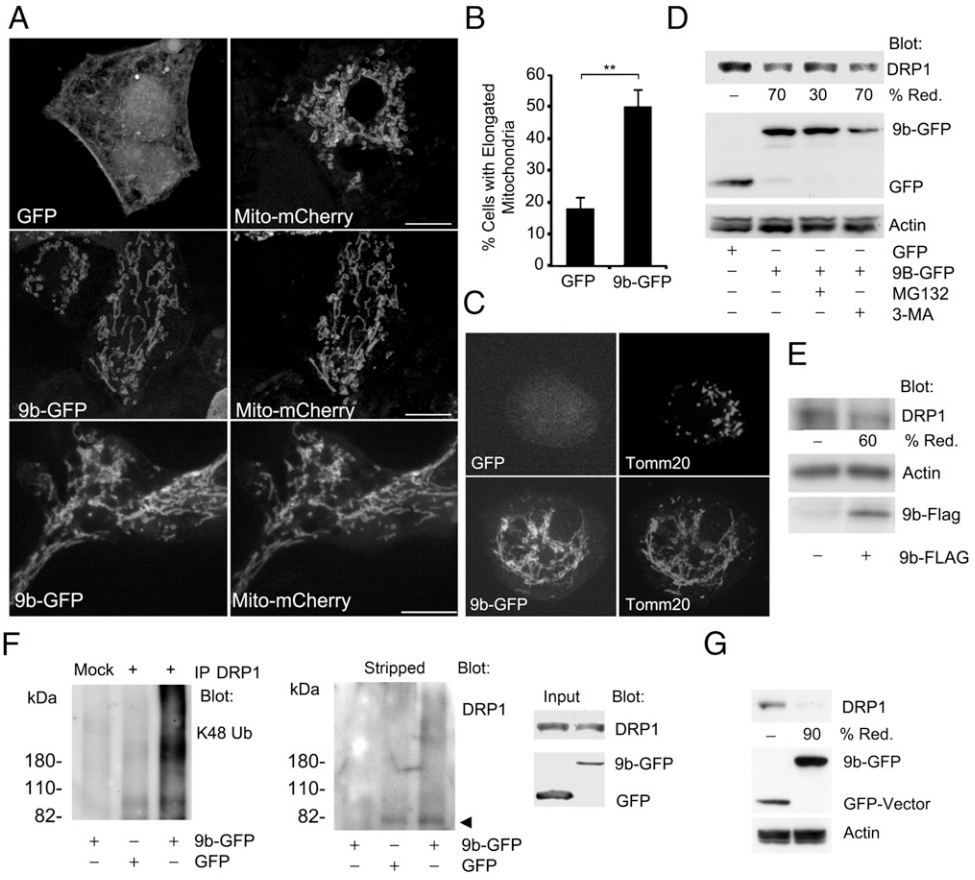

FIGURE 1. ORF-9b expression elongates mitochondria and enhances the degradation of DRP1. (**A**) Confocal microscopy of A549 cells expressing GFP (*top*) or 9b-GFP (*middle*) and mito-mCherry or HEK 293 cells expressing 9b-GFP and mito-mCherry (*lower*). Individual images are shown. Scale bar, 10 μm. (**B**) Quantitation of percentage of cells with elongated mitochondria in A549 cells expressing GFP or 9b-GFP and Mito-mCherry. Coexpressing cells (100 each) were imaged, and percentage of cells with obviously elongated mitochondria was enumerated. $^{**}p < 0.01$. (**C**) Confocal microscopy of THP-1 cells permanently expressing 9b-GFP or GFP and immunostained for Tomm20. Original magnification ×1000. (**D**) Immunoblot of cell lysates from HEK 293 cells expressing GFP or 9b-GFP to detect DRP1. In some instances, the cells were treated with MG-132 (10 μM) or 3-MA (5 mM) for 4 h. (**E**) Immunoblots of cell lysates from HEK 293 cells transfected with Flag or 9b-Flag for indicated proteins. (**F**) Immunoblots of DRP1 immunoprecipitates (+) and cell lysates from HEK 293 cells transfected with GFP or 9b-GFP. The mock lane is a control Ab immunoprecipitation. Following the K48 ubiquitin (Ub) immunoblot, the membrane was stripped and reblotted for DRP1. The cells were treated with MG-132 for the last 4 h prior to cell lysis. (**G**) Immunoblot of cell lysates from THP-1 cells permanently expressing either 9b-GFP or GFP to detect DRPl.

SARS-CoV (32). Mitochondrial-localized MAVS links mitochondria to antiviral type I IFN signaling. Because SARS-CoV–infected cells have impaired IFN responses (18) and ORF9b localized to mitochondria, we checked whether ORF-9b impacted MAVS signaling. We expressed 9b-GFP in the presence of either an IFN-β or a NF-κB reporter construct and simulated an intracellular viral infection by cotransfecting poly(I:C). As expected, poly(I:C) induced both reporter constructs, but the presence of ORF-9b significantly inhibited this response (Fig. 3A). Next, we tested where in the signaling pathway ORF-9b acted by assessing reporter gene activation following expression of a constitutively active form of RIG-I (RIG-$I^{1–250}$) or by MAVS overexpression (33). In both instances, ORF-9b reduced the activation of the reporters, arguing that ORF-9b functions at the level of MAVS or more distally (Fig. 3A). We verified that the 9b-Flag construct also inhibited MAVS signaling (Fig. 3B). Because MAVS is required for the phosphorylation of IRF3 in the RIG-I–mediated antiviral response, we checked whether 9b-GFP expression reduced IRF3 phosphorylation, which it did (Fig. 3C). Next, we measured IFN-β levels by immunoblotting cell supernatants conditioned by THP1 cells transfected with Myc-MAVs in the presence or absence of 9b-Flag. As expected, the amount of IFN-β decreased in the cell supernatant in the presence of 9b-Flag (Fig. 3D). In contrast, ORF-9b had little impact on IFN-β production in THP-1 cells triggered by either exposing the cells to a TLR3 ligand (Fig. 3E) or transfecting the cells with an IRF-3 expression vector (Fig. 3F). Next, we determined whether ORF-9b and MAVS could be found in the same molecular complex. We found that expressed 9b-GFP consistently immunoprecipitated with endogenous MAVS (Fig. 3G). Mapping the region in MAVS needed to coimmunoprecipitate with ORF-9b suggested that the mitochondrial membrane insertion sequence in MAVS (aa 514–535) was necessary. However, the 503–540 MAVS construct coimmunoprecipitated less well than full-length MAVS, implying that another region in MAVS may be needed (Fig. 3H). We also checked whether the reduction of DRP1 noted above might contribute to the impaired induction of IFN-β. We used a previously described shRNA to reduce DRP1 levels in HEK 293 cell (34). Lowered DRP1 levels impaired the MAVS-induced increased IFN-β reporter activity, although not nearly as effectively as did the 9b-FLAG construct (Fig. 3I). The DRP1 shRNA appropriately decreased DRP1 expression, but did not impact endogenous MAVS expression (Fig. 3J). This indicates that the ORF-9b–mediated reduction in DRP1 may contribute to the decrease in type I IFN signaling; however, other mechanisms must be operant.

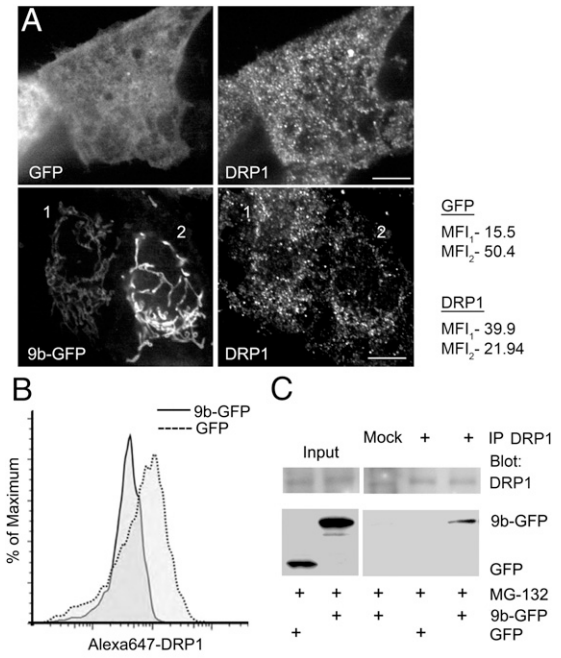

FIGURE 2. ORF-9b expression leads to less DRP1 associated with mitochondria and ORF-9b coimmunoprecipitates with DRP1. (**A**) Confocal microscopy of endogenous DRP1 in A549 cells transiently transfected with GFP-ORF9b or GFP vector alone. Scale bar, 10 μm. Mean fluorescence intensity (MFI) of DRP1 or GFP was quantified from the whole volume using ImageJ for cell 1 and cell 2. (**B**) Flow cytometry analysis of endogenous DRP1 level in A549 cells expressing either GFP or 9b-GFP. The mean fluorescent intensity of DRP1 in GFP^+ cells was 186 and 46 in the 9b-GFP^+ cells. (**C**) Immunoblots of DRP1 immunoprecipitates (+) and cell lysates from HEK 293 cells transfected with GFP or 9b-GFP for indicated proteins. Mock is a control Ab immunoprecipitation. Cells were treated with MG-132 (10 μM).

To check whether ORF-9b altered the intracellular distribution of MAVS, we expressed 9b-GFP in A549 cells and immunostained for endogenous MAVS. Standard confocal microscopy revealed that, in 9b-GFP–expressing cells, MAVS had a more punctate appearance forming small aggregates along 9b-GFP–delineated mitochondria (Fig. 4A). This is most evident in the zoomed images shown in the *insets* (Fig. 4A). To better visualize the distribution of MAVS in the control and ORF-9b–expressing cells, we used STED microscopy. In the control cell, most of the MAVS distributed uniformly along mitochondria-like structures, whereas small, discrete MAVS puncta distributed along elongated ORF-9b–delineated mitochondria (green in the *inset*, Fig. 4B). Although this is a subjective conclusion, it is based on the examination of numerous images. We also examined the localization of MAVS and ORF-9b by immunoelectron microscopy and observed the apposition of Flag-tagged ORF-9b (9b-Flag) with endogenous MAVS at the outer mitochondrial membrane (Fig. 4C, 4D). These data indicate that ORF-9b is in close physical association with MAVS.

SARS-CoV ORF-9b limits IFN signaling by degrading the MAVS signalosome

We had noted the level of the epitope-tagged MAVS was reduced in the ORF-9b–expressing cells compared with the level in control cells, so we checked endogenous MAVS levels following 9b-GFP expression. We found that, following 9b-GFP expression, the level of endogenous MAVS, as determined by immunoblotting, had declined by ~50%. The reduction was partially reversed by a proteasomal inhibitor, but not by an autophagy inhibitor (Fig. 5A). Because MAVS recruits TRAF3 and TRAF6 to activate downstream signaling pathways, we also checked whether ORF-9b expression affected their expression. To do so, we immunoblotted cell lysates prepared from HEK 293 cells expressing epitope-tagged versions of TRAF3 or TRAF6 along with either GFP or 9b-GFP (Fig. 5B). Surprisingly, the reductions in the epitope-tagged TRAF3 and TRAF6 equaled those of Myc-MAVS. Indicating that ORF-9b most likely triggers K48-linked ubiquitination of MAVS immunoblotting, Myc-MAVS immunoprecipitates revealed the presence of K48-linked ubiquitin (Fig. 5C). This last experiment was done using a stringent protocol that reduces the likelihood that the immunoprecipitates will contain spurious proteins (28, 35). Stripping the membrane and reblotting with Abs directed at the Myc tag revealed a smeared band also suggestive of MAVS ubiquitination (Fig. 5C). We verified that 9b-Flag also reduced Myc-MAVS levels (Fig. 5D). Finally, in the THP-1 cells permanently transfected with 9b-GFP, we also found a marked reduction in the endogenous level of MAVS (Fig. 5E). These results led us to search for the E3 ligase responsible for ubiquitinating MAVS following ORF-9b expression.

It is known that PCBP2 acts as a gatekeeper to control MAVS levels and signaling by linking the AIP4 E3 ubiquitin ligase with MAVS (27). To determine whether ORF-9b usurped PCBP2 and AIP4 to degrade MAVS, we reduced their levels in cells that expressed 9b-GFP. We found that the two shRNAs partially reversed the ORF-9b–mediated reduction in MAVS (Fig. 6A). In addition, endogenous PCBP2 could pull down 9b-GFP and endogenous MAVS, suggesting that ORF-9b may form a trimolecular complex (Fig. 6B). Next, we reduced PCBP2 or AIP4 expression, and we checked poly(I:C)-induced reporter gene activation in the presence of 9b-GFP (Fig. 6C). We found that reducing either PCBP2 or AIP4 largely reversed the ORF-9b–mediated inhibition of poly(I:C)-induced reporter gene activity. Together, these data indicate that ORF-9b targets several members of the MAVS signalosome for destruction. It largely does so by recruiting PCBP2 and the AIP4 E3 ligase. As a consequence, MAVS, TRAF3, and TRAF6 levels decline in the host cell, limiting the cells' ability to generate a potent IFN response to viral RNA.

SARS-CoV ORF-9b promotes the formation of autophagosomes

Finally, because mitochondrial damage and changes in mitochondrial morphology have been linked to autophagy, and many CoV trigger autophagy (36), we checked autophagy levels in 9b-GFP–expressing cells by coexpressing the autophagy marker LC3-tagged RFP (LC3-RFP) in A549 cells. When autophagosomes form, LC3-RFP is processed and recruited to the autophagosomal membrane, resulting in the accumulation of fluorescent cytoplasmic dots. Interestingly, 9b-GFP expression potently induced autophagosome formation in A549 cells (Fig. 7A, Supplemental Video 2). The video shows numerous interactions between elongated mitochondria and autophagosomes. Similarly, 9b-Flag triggered autophagy in the same cells (Fig. 7B). Quantification of the imaging, electron microscopy, and LC3 immunoblotting confirmed the increase in autophagosome formation (Fig. 7C–E). The electron microscopy also revealed the mitochondrial morphology changes noted previously and a close association between mitochondria and the autophagosomes (Fig. 7D). The induction of autophagy by ORF-9b depended upon ATG5, an important regulator of autophagosome formation, as reducing its expression decreased 9b-GFP–triggered LC3 processing (Fig. 7F). Although ATG5–ATG12 conjugates can interact with MAVS to impair its antiviral effects (37), reducing ATG5 expression did not

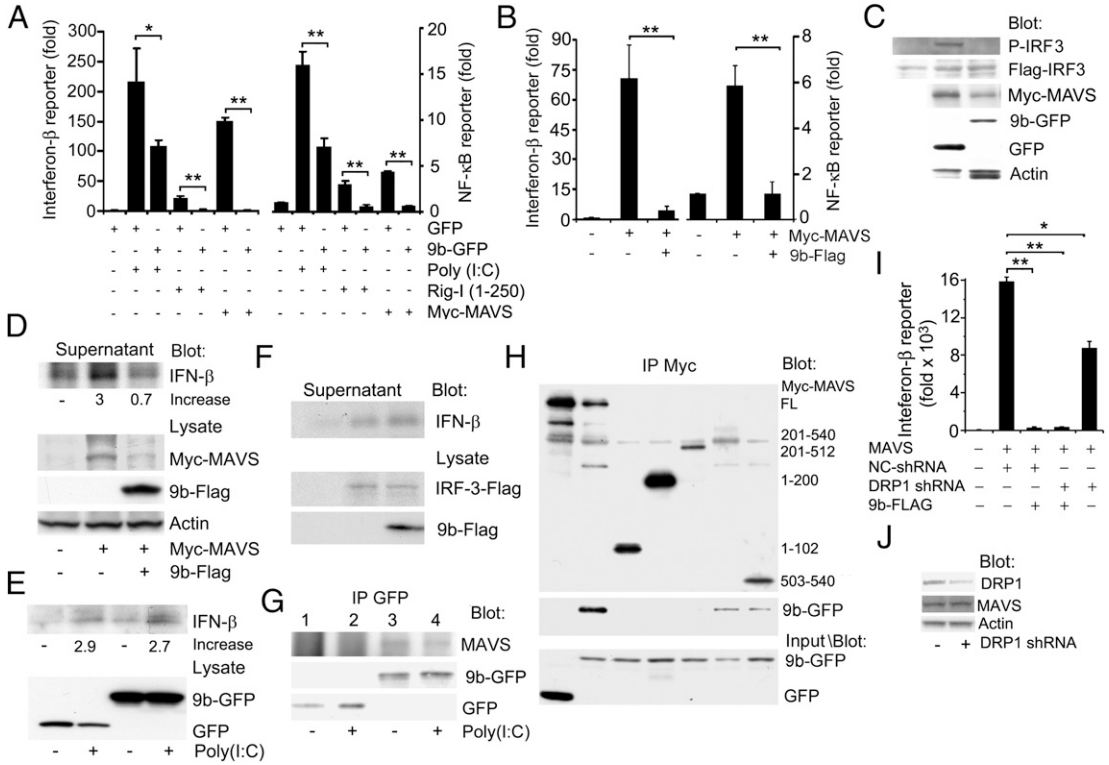

FIGURE 3. ORF-9b inhibits antiviral type I IFN responses. (**A**) IFN-β and NF-κB reporter gene assays using HEK 293 cells expressing GFP or 9b-GFP and induced by transfection of poly(I:C), RIG-I$^{1-250}$, or MAVS. Luciferase activity is shown as fold induction. (**B**) IFN-β and NF-κB reporter gene assays using HEK 293 cells expressing Flag or 9b-Flag and induced by transfection of myc-MAVS. Luciferase activity is shown as fold induction. (**C**) Immunoblot of HEK 293 cells expressing Flag-IRF3 and Myc-MAVS and either GFP or 9b-GFP to detect phosphorylated (P)-IRF-3. (**D**) Immunoblot of IFN-β in cell supernatants and indicated proteins in cell lysates from THP-1 transiently transfected with Myc-MAVS and expressing 9b-Flag or not. (**E**) Immunoblot of IFN-β and indicated proteins in cell lysates from THP-1 permanently expressing GFP or 9b-GFP and exposed to poly(I:C) overnight (10 μg/ml). (**F**) Immunoblots of IFN-β in cell supernatants and of the indicated proteins in cell lysates from THP-1 cells transiently transfected with an IRF-3 expression vector. (**G**) Immunoblot of GFP immunoprecipitates from HEK 293 cells expressing GFP vector or ORF-9b-GFP for endogenous MAVS. Poly(I:C) was transfected 1 h prior to cell lysis. (**H**) Immunoblot of Myc immunoprecipitates from HEK 293 cells expressing full-length or truncated Myc-MAVS and GFP or 9b-GFP. GFP and 9b-GFP expression levels were verified by immunoblotting cell lysates from the same cells. (**I**) IFN-β reporter assays using HEK293 cells expressing a control (NC) or a DRP1 shRNA in the presence or absence of 9b-FLAG. MAVS expression was used to induce reporter gene activity. (**J**) Immunoblot verifying that the DRP1 shRNA reduced DRP1 expression, but did not affect endogenous MAVS expression. $*p < 0.05$, $**p < 0.01$ by t test.

appreciably impact MAVS signaling in the presence or absence of 9b-GFP (Fig. 7H). This indicates that the increased autophagy in ORF-9b expressing minimally contributes to the previously noted loss of MAVS signaling. We also checked the basal autophagy levels in the THP-1 cells permanently transfected with either 9b-GFP or GFP. Although we noted an increase in LC3 processing in the 9b-GFP–expressing cells compared with control cells, the difference was small (Fig. 7G). This suggests that the cells had compensated for the prolonged ORF-9b expression or that some intrinsic difference exists between macrophages and the other cell types.

Discussion

Our observations indicate the SARS-CoV ORF-9b provides a receptive intracellular environment for viral replication by targeting the mitochondrial MAVS signalosome. ORF-9b localizes to mitochondria, where it promotes mitochondrial elongation by enhancing DRP1 degradation. In the presence of ORF-9b, MAVS becomes concentrated into small puncta and subject to PCBP2 and AIP4 ubiquitination. The degradation of MAVS is accompanied by a loss of TRAF3 and TRAF6, two key signaling intermediaries in antiviral defenses. In addition, acute ORF-9b expression results in ATG5-dependent autophagosome formation.

The expression of ORF-9b in A549, HEK 293, and THP-1 cells resulted in a rather striking set of cellular changes. ORF-9b localized to mitochondria and led to mitochondrial elongation. This is in contrast to the usual mitochondrial fragmentation that occurs following viral infection and, to our knowledge, has not been reported with another viral ORF. Mitochondrial elongation has been reported following infection of cells with a defective strain of Sendai virus. The mitochondrial elongation was linked to RLR activation and enhanced MAVS signaling (38). This differed from ORF-9b expression, which also caused mitochondrial elongation, but severely limited MAVS signaling. In contradistinction to the defective virus, the wild-type Sendai virus triggered mitochondrial fragmentation and aggregation (38). Similarly, hepatitis C virus infection caused mitochondrial perinuclear clustering, the translocation of Parkin to mitochondria, and mitophagy (39). Perhaps ORF-9b counteracts the impact of other cellular stresses during SARS-CoV infection, which fragment and aggregate mitochondria, thereby helping to promote cell survival during viral replication. Mitochondrial fusion is known to protect mitochondria from starvation-induced autophagosomal degradation (40, 41).

Our localization results differ from those previously reported localization results of ORF-9b in Vero cells (16, 17). We observed a similar localization of ORF-9b in three different human cell types using both Flag- and GFP-tagged versions. We show mitochondrial localization in all three cell types and failed to see a visible accumulation of ORF-9b in the nucleus of any of three

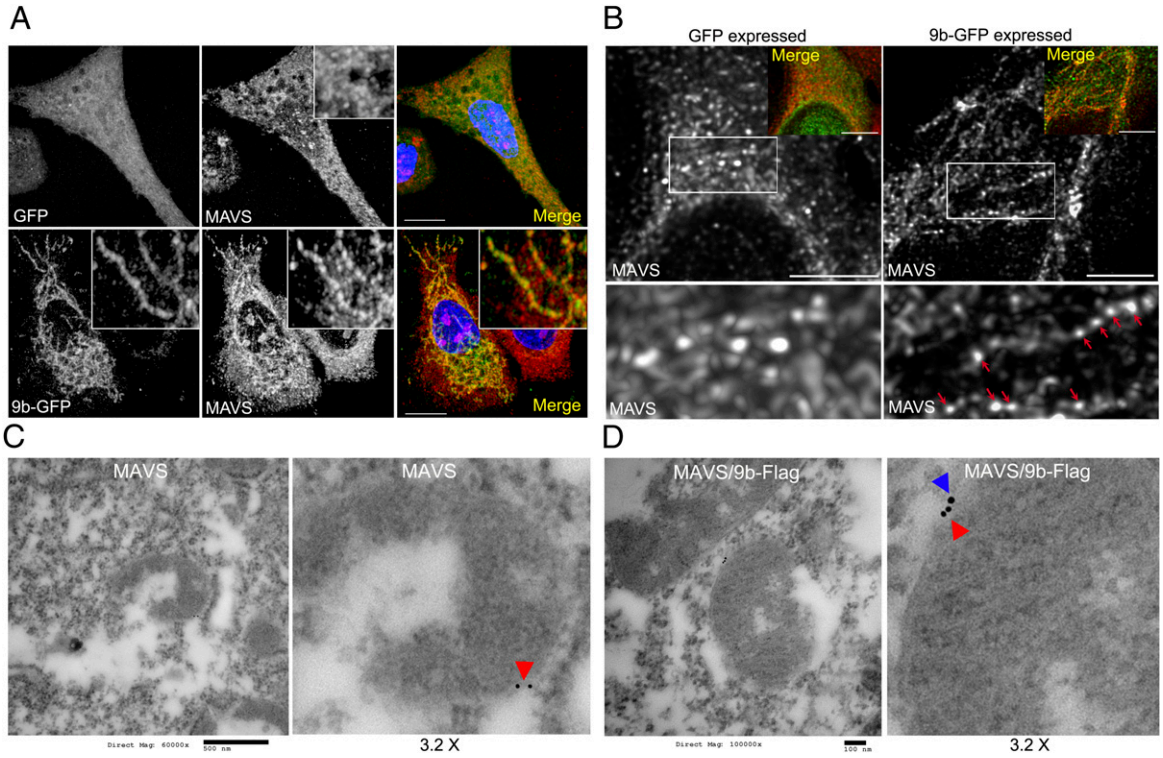

FIGURE 4. Imaging ORF-9b expression reveals ORF-9b and MAVS colocalized and increased MAVS aggregation. (**A**) Images from confocal microscopy of A549 cells expressing GFP or 9b-GFP immunostained for MAVS (red) and labeled with DNA dye (blue). *Inset*, 3× electronic zoom. Scale bar, 10 μm. (**B**) Images from STED microscopy of A549 cells expressing 9b-GFP and immunostained for MAVS. The 9b-GFP was imaged by confocal microscopy. Overlap is shown as an *inset*. Scale bar, 2 μm. Below each image is a 2.5× electronic zoom of the white boxed area. Red arrows indicate MAVS accumulation along 9b-GFP–delineated mitochondria. (**C**) Immunoelectron microscopy of HEK 293 cells transfected with a control vector and immunostained for MAVS (red arrowhead). Scale bar, 500 nM. *Right image* is a 3.2× electronic zoom of the mitochondria in the *left image*. (**D**) Immunoelectron microscopy of HEK 293 cells transfected with 9b-Flag and immunostained for MAVS (red arrowhead) and Flag (blue arrowhead). Scale bar, 100 nM. *Right image* is a 3.2× electronic zoom of the mitochondria in the *left image*.

cell types. The mitochondrial localization reported in this work was confirmed by life cell imaging of cells coexpressing Mitotracker and by immunostaining fixed cells for Tomm20 and MAVS. The two other studies did not look for mitochondria lo-

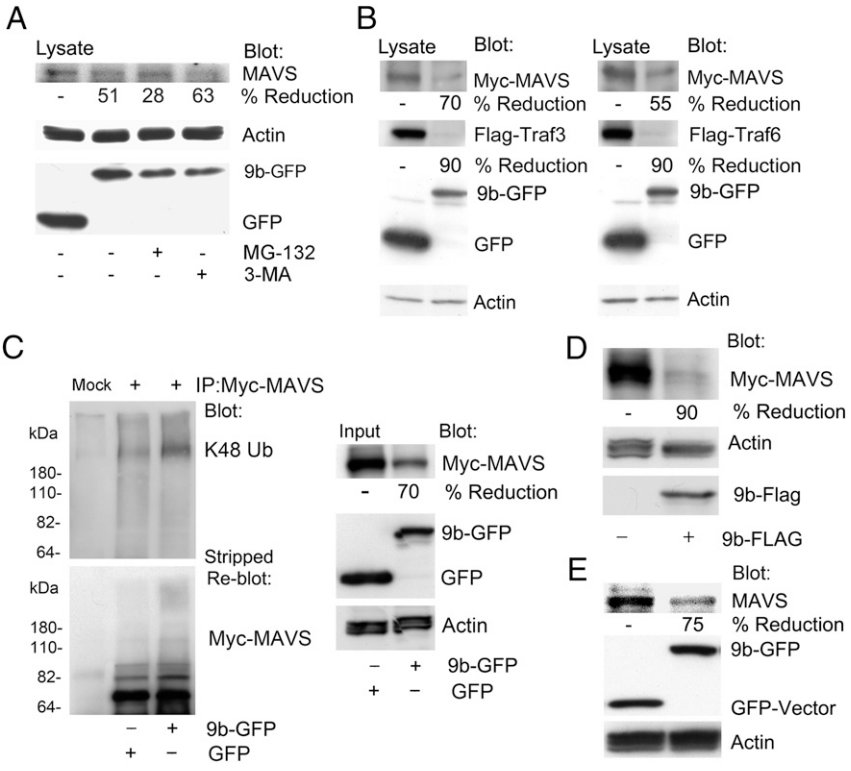

FIGURE 5. ORF-9b enhances MAVS proteasomal degradation via its K48-linked ubiquitination. (**A**) Immunoblots of lysates from HEK 293 cells expressing GFP vector or 9b-GFP untreated or treated with MG-132 (10 μM) or 3-MA (5 mM) for 4 h. The blots show the indicated proteins. (**B**) Immunoblots of lysates from HEK 293 cells expressing Flag-TRAF3 or Flag-TRAF6 and either GFP or 9b-GFP. The blots show the indicated proteins. (**C**) Immunoblots of Myc immunoprecipitates (+) and cell lysates from HEK 293 cells expressing Myc-MAVS and GFP or 9b-GFP. Following immunoblotting for K48 ubiquitin (Ub), the membrane was stripped and probed for Myc-MAVS. Mock is a control Ab immunoprecipitation. (**D**) Immunoblots of lysates from HEK 293 cells expressing Myc-MAVS in the presence of either the Flag-vector or 9b-Flag. The blots show the indicated proteins. (**E**) Immunoblots of lysates from THP-1 cells permanently expressing GFP or 9b-GFP for endogenous MAVS. Also shown are GFP, 9b-GFP, and actin levels.

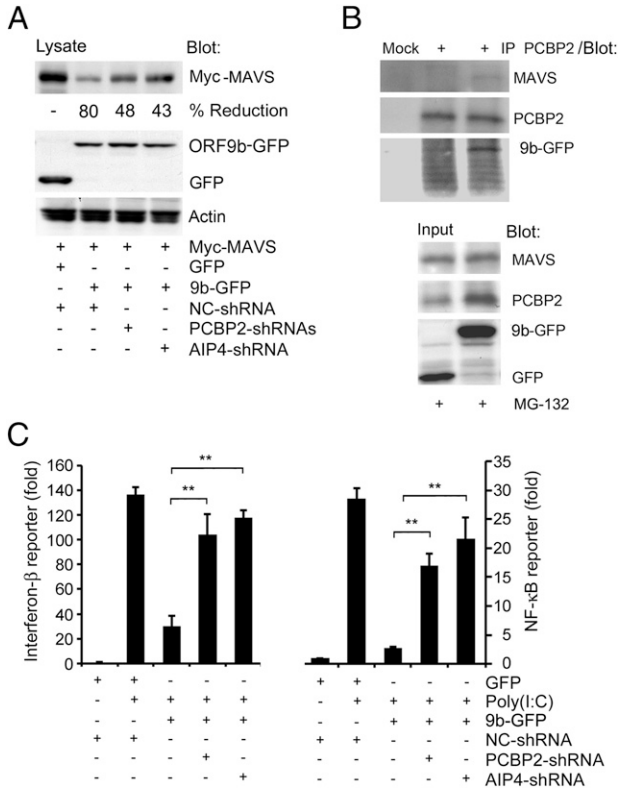

FIGURE 6. ORF-9b uses PCBP2/AIP4 to degrade MAVS and to impair type I IFN responses. (**A**) Immunoblot of lysates from HEK 293 cells expressing Myc-MAVS and either GFP or 9b-GFP in the presence of a control shRNA or a shRNA targeting either PCBP2 or AIP4. (**B**) Immunoblot of cell lysates and PCBP2 immunoprecipitates (+) from HEK 293 cells expressing GFP or 9b-GFP. Cells were treated with MG-132 (10 μM) for 2 h prior to lysis. Mock is a control Ab immunoprecipitation. (**C**) IFN-β and NF-κB reporter assays using HEK 293 cells expressing GFP or 9b-GFP along with a control, PCBP2, or AIP4 shRNA and induced by transfection of poly(I:C). The luciferase activity shows in fold induction. Statistics analyzed by *t* test. $^{**}p < 0.01$.

calization. As mitochondria are often closely associated with the endoplasmic reticulum, the colocalization of ORF-9b with an endoplasmic marker may have obscured its true localization. Less likely is that the localization of ORF-9b has a cell type–dependent distribution pattern.

In the ORF-9b–expressing cells, DRP1 levels declined as a consequence of ubiquitination and proteasomal degradation, most likely explaining the change in mitochondria morphology. Parkin is an E3 ligase that is known to ubiquitinate DRP1 for proteasome-dependent degradation. Reducing Parkin expression in HeLa cells enhanced DRP1 levels and caused mitochondrial fragmentation (42). To test whether ORF-9b used Parkin to ubiquitinate DRP1, we reduced its expression and examined the mitochondrial morphology in the knockdown cells. The reduced Parkin expression did not alter the mitochondrial morphology changes triggered by ORF-9b expression, arguing that another E3 ligase ubiquitinates DRP1 following ORF-9b expression (C. Shi, unpublished result). We also considered whether autophagosomal degradation contributed to the reduced DRP1 levels noted in ORF-9b–expressing cells. Inhibitors of autophagy increased DRP1 levels in HEK 293T cells, and increasing autophagy reduced DRP1 levels in neurons (43); however, an autophagy inhibitor did not reverse the lowered DRP1 levels observed in the ORF-9b–expressing cells.

SARS-CoV ORF-9b most likely has little role in directly supporting viral replication, but rather its primary function is to inactivate the RLR pathway by triggering degradation of the MAVS/TRAF3/TFAF6 signalosome. As mentioned in the introductory section, RNA viruses have evolved several different mechanisms to disable MAVS signaling, including cleaving MAVS from the mitochondria (24), assembling a degradasome (26), and usurping a host cell-negative regulatory system, the AIP4-PCBP2-MAVS axis, as we describe in this work. PCBP2 serves as an adapter molecule recruited to mitochondrial MAVS following viral infection or MAVS overexpression (27). The C-terminal portion of MAVS is needed to recruit PCBP2 and ORF-9b. Following ORF-9b expression, we found that PCBP2 immunoprecipitates contained both MAVS and ORF-9b. This suggests the localization of ORF-9b to the mitochondria had led to the translocation of PCBP2 from the nucleus to the mitochondria. Rescue of the ORF-9b phenotype by knockdown of PCBP2 also indicates that ORF-9b expression had led to PCBP2 recruitment to mitochondria. Although the physiologic signal that triggers PCBP2 nuclear export and its localization to mitochondria following viral infection is unknown, mitochondria are a logical source. Pathogenic viral infections cause mitochondrial stress. Stressed mitochondria release reactive oxygen species and a variety of other mediators and affect intracellular calcium levels. However, mitochondrial stress typically causes mitochondrial fission, not mitochondria fusion (44), as we noted in the ORF-9b–expressing cells.

Not only did we observe a strong reduction in MAVS levels following ORF-9b expression, but also in two key signaling intermediates, TRAF3 and TRAF6. Because reducing either AIP4 or PCBP2 expression largely rescued the ORF-9b–induced signaling defect, the TRAF3 and TRAF6 levels are likely to have been restored. It is unlikely that TRAF3 and TRAF6 are direct targets of the PCBP2/AIP4, but rather are indirectly targeted for destruction by their association with MAVS. Whereas TRAF3 is directly targeted by the E3 ligase Triad3, which also negatively regulates MAVS signaling, Triad3 does not cause MAVS degradation (45). The viral degradasome induced by the expression of respiratory syncytial virus NS1 proteins results in the degradation of a number of proteins in the IFN induction and response pathway, including RIG-I, TRAF3, and IRF3, but MAVS was not one of them (26). Our current studies are aimed at understanding how ORF-9b expression recruits PCBP2/AIP4 and determining how TRAF3 and TRAF6 are also degraded. Our working hypothesis is that the ORF-9b/MAVS interaction triggered a partial assembly of the MAVS/TRAF3/TRAF6 signalosome, which leads to a signal that recruits PCBP2/AIP4. As a consequence, MAVS and perhaps other proteins are ubiquitinated and delivered to the proteasome for degradation.

Although the observed decreases in DRP1 and MAVS/TRAF3/TRAF6 can explain the mitochondrial elongation and reduced antiviral signaling in the ORF-9b expressing, we have not found an immediately proximal cause of the increase autophagy in HEK293 and A549 cells. Given its localization to mitochondria, mitochondria involvement in the enhanced autophagy noted in the ORF-9b–expressing cells seems likely. However, whereas mitochondrial damage and increased mitochondrial reactive oxygen species production are known triggers for autophagosome formation, they had no clearly defined role in this work. Because the mitochondrial potential in control and ORF-9b–expressing cells did not differ, mitochondrial reactive oxygen species production is an unlikely culprit. We also examined autophagy as assessed by LC3 immunoblotting in the THP-1 cells permanently transfected with ORF-9b. Although we observed a small increase in LC3 processing in the ORF-9b–expressing cells, the difference was less

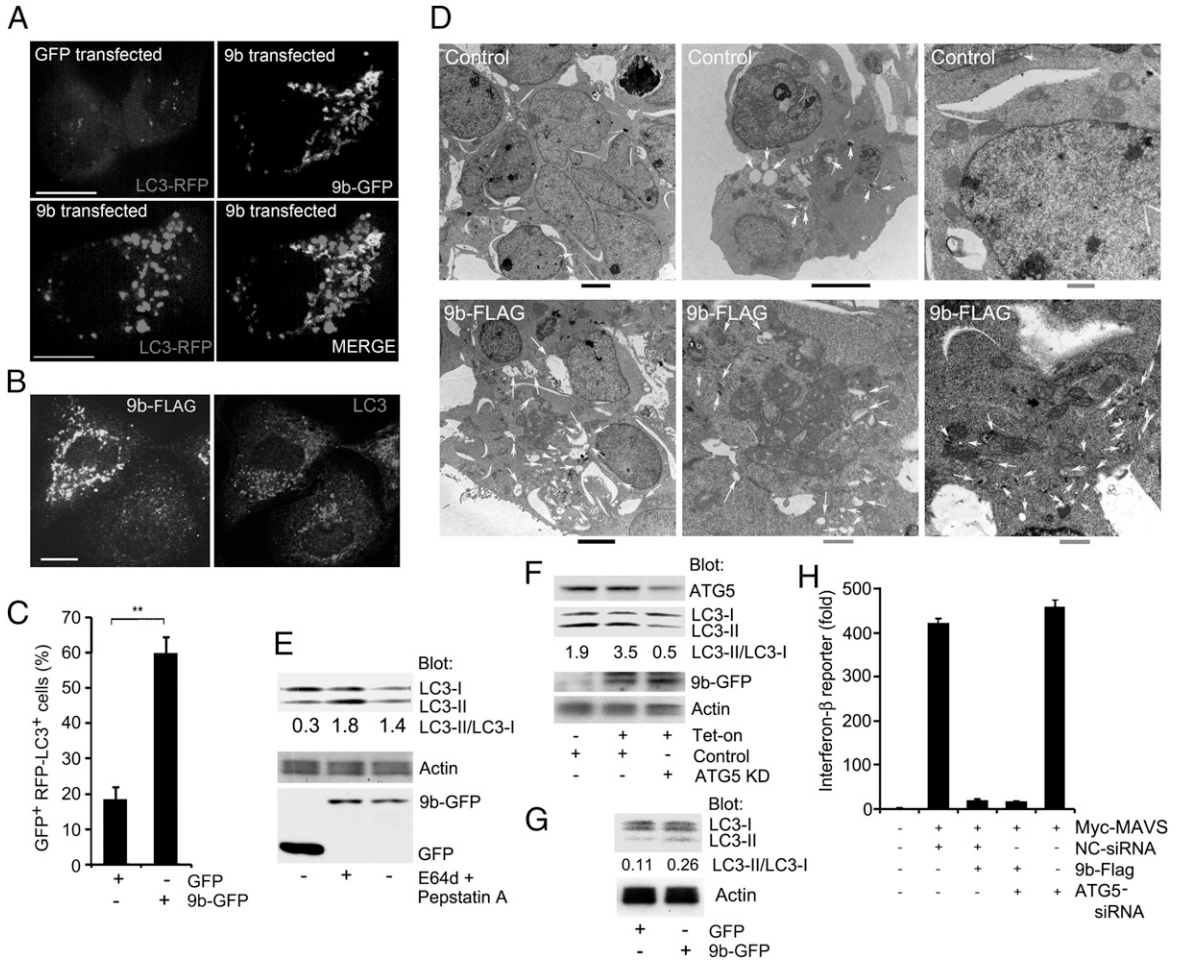

FIGURE 7. ORF-9b induces autophagy. (**A**) Images from confocal microscopy of A549 cells coexpressing GFP vector or 9b-GFP with LC3-RFP. Individual and merged images are shown as indicated. Scale bar, 10 μm. (**B**) Images from confocal microscopy of A549 cells expressing 9b-Flag and immunostained for endogenous LC3 and Flag. Individual images are shown. Scale bar, 10 μm. (**C**) The number of GFP-positive cells with >10 LC3-RFP puncta in A549 cells based on the imaging from (A). $^{**}p < 0.01$, *t* test. (**D**) Images from electron microscopy of HEK 293 cells expressing a control (*top three images*) or 9b-Flag (*bottom three images*). Arrows mark the autophagosomes. Black scale bars, 4 μm; gray scale bars, 1 μm. (**E**) Immunoblot of lysates from A549 cells expressing GFP or 9b-GFP for the indicated proteins. The lysosome inhibitors E64d and pepstatin A were added, as indicated, for the last 4 h. The ratio of LC3-II/LC3-I is shown. (**F**) Immunoblot of cell lysates from A549 cells expressing 9b-GFP under tetracycline control expressing an ATG5 siRNA or not. The cells were tetracycline induced for 16 h prior to cell lysis. The ratio of LC3-II/LC3-I is shown. (**G**) Immunoblot of cell lysates from THP-1 permanently expressing GFP or 9b-GFP. The ratio of LC3-II/LC3-I is shown. (**H**) IFN-β reporter assay using HEK 293 cells expressing Flag or 9b-Flag along with Myc-MAVS and control or ATG5 siRNAs. Luciferase activity is shown as fold induction.

marked than what we had observed following the acute expression of ORF-9b in A549 and HEK 293 cells. Further studies will be needed to delineate the mechanisms by which ORF-9b triggers marked autophagosome formation in some cell types and not others.

We also considered whether the enhanced autophagy in A549 and HEK 293 cells might contribute to the reduced MAVS activity that we observed. Previous studies have shown that some viruses activate the autophagy pathway to reduce MAVS signaling and impair antiviral responses (46, 47). Furthermore, the ATG5–ATG12 conjugate has been shown to negatively regulate the type I IFN production pathway by direct association with RIG-I and IFN-β promoter stimulator 1 (37). However, in our hands, ORF-9b–mediated suppression of MAVS signaling did not depend upon the autophagy factor ATG5, as reducing its expression did not impact the suppression in antiviral signaling. In addition, the pharmacological inhibition of autophagy did not reverse the loss of MAVS following ORF-9b expression. The modest increase in autophagy in the 9b-GFP–expressing THP-1 despite a potent reduction in MAVS expression also argues that the induction of autophagy did not contribute to the loss of MAVS and MAVS signaling that we noted.

Finally, the ORF-9b–mediated loss of MAVS may further limit host innate responses by reducing NLRP3 inflammasome activity, as MAVS promotes NLRP3 mitochondrial localization and inflammasome activation (48). We are currently testing whether the expression of ORF-9b also affects inflammasome activity by targeting NLRP3 levels. In conclusion, SARS-CoV uses ORF-9b to target host cell mitochondria to disable MAVS signaling. Our data support the use of IFN-α therapy as a prophylactic treatment against SARS-CoV, but suggest that it will be less effective when administered to patients with an established infection.

Acknowledgments

We thank Dr. Anthony S. Fauci for continued support.

Disclosures

The authors have no financial conflicts of interest.

References

1. Drosten, C., S. Günther, W. Preiser, S. van der Werf, H. R. Brodt, S. Becker, H. Rabenau, M. Panning, L. Kolesnikova, R. A. Fouchier, et al. 2003. Identification of a novel coronavirus in patients with severe acute respiratory syndrome. *N. Engl. J. Med.* 348: 1967–1976.
2. Peiris, J. S., S. T. Lai, L. L. Poon, Y. Guan, L. Y. Yam, W. Lim, J. Nicholls, W. K. Yee, W. W. Yan, M. T. Cheung, et al; SARS Study Group. 2003. Coronavirus as a possible cause of severe acute respiratory syndrome. *Lancet* 361: 1319–1325.
3. Ksiazek, T. G., D. Erdman, C. S. Goldsmith, S. R. Zaki, T. Peret, S. Emery, S. Tong, C. Urbani, J. A. Comer, W. Lim, et al; SARS Working Group. 2003. A novel coronavirus associated with severe acute respiratory syndrome. *N. Engl. J. Med.* 348: 1953–1966.
4. Peiris, J. S., Y. Guan, and K. Y. Yuen. 2004. Severe acute respiratory syndrome. *Nat. Med.* 10: S88–S97.
5. Stadler, K., V. Masignani, M. Eickmann, S. Becker, S. Abrignani, H. D. Klenk, and R. Rappuoli. 2003. SARS—beginning to understand a new virus. *Nat. Rev. Microbiol.* 1: 209–218.
6. Hilgenfeld, R., and M. Peiris. 2013. From SARS to MERS: 10 years of research on highly pathogenic human coronaviruses. *Antiviral Res.* 100: 286–295.
7. Balboni, A., M. Battilani, and S. Prosperi. 2012. The SARS-like coronaviruses: the role of bats and evolutionary relationships with SARS coronavirus. *New Microbiol.* 35: 1–16.
8. Zaki, A. M., S. van Boheemen, T. M. Bestebroer, A. D. Osterhaus, and R. A. Fouchier. 2012. Isolation of a novel coronavirus from a man with pneumonia in Saudi Arabia. *N. Engl. J. Med.* 367: 1814–1820.
9. Butler, D. 2012. SARS veterans tackle coronavirus. *Nature* 490: 20.
10. Rota, P. A., M. S. Oberste, S. S. Monroe, W. A. Nix, R. Campagnoli, J. P. Icenogle, S. Peñaranda, B. Bankamp, K. Maher, M. H. Chen, et al. 2003. Characterization of a novel coronavirus associated with severe acute respiratory syndrome. *Science* 300: 1394–1399.
11. Marra, M. A., S. J. Jones, C. R. Astell, R. A. Holt, A. Brooks-Wilson, Y. S. Butterfield, J. Khattra, J. K. Asano, S. A. Barber, S. Y. Chan, et al. 2003. The genome sequence of the SARS-associated coronavirus. *Science* 300: 1399–1404.
12. McBride, R., and B. C. Fielding. 2012. The role of severe acute respiratory syndrome (SARS)-coronavirus accessory proteins in virus pathogenesis. *Viruses* 4: 2902–2923.
13. Meier, C., A. R. Aricescu, R. Assenberg, R. T. Aplin, R. J. Gilbert, J. M. Grimes, and D. I. Stuart. 2006. The crystal structure of ORF-9b, a lipid binding protein from the SARS coronavirus. *Structure* 14: 1157–1165.
14. Qiu, M., Y. Shi, Z. Guo, Z. Chen, R. He, R. Chen, D. Zhou, E. Dai, X. Wang, B. Si, et al. 2005. Antibody responses to individual proteins of SARS coronavirus and their neutralization activities. *Microbes Infect.* 7: 882–889.
15. Chan, W. S., C. Wu, S. C. Chow, T. Cheung, K. F. To, W. K. Leung, P. K. Chan, K. C. Lee, H. K. Ng, D. M. Au, and A. W. Lo. 2005. Coronaviral hypothetical and structural proteins were found in the intestinal surface enterocytes and pneumocytes of severe acute respiratory syndrome (SARS). *Mod. Pathol.* 18: 1432–1439.
16. Moshynskyy, I., S. Viswanathan, N. Vasilenko, V. Lobanov, M. Petric, L. A. Babiuk, and A. N. Zakhartchouk. 2007. Intracellular localization of the SARS coronavirus protein 9b: evidence of active export from the nucleus. *Virus Res.* 127: 116–121.
17. Sharma, K., S. Åkerström, A. K. Sharma, V. T. Chow, S. Teow, B. Abrenica, S. A. Booth, T. F. Booth, A. Mirazimi, and S. K. Lal. 2011. SARS-CoV 9b protein diffuses into nucleus, undergoes active Crm1 mediated nucleocytoplasmic export and triggers apoptosis when retained in the nucleus. *PLoS One* 6: e19436.
18. Spiegel, M., A. Pichlmair, L. Martínez-Sobrido, J. Cros, A. García-Sastre, O. Haller, and F. Weber. 2005. Inhibition of beta interferon induction by severe acute respiratory syndrome coronavirus suggests a two-step model for activation of interferon regulatory factor 3. *J. Virol.* 79: 2079–2086.
19. Cinatl, J., Jr., M. Michaelis, M. Scholz, and H. W. Doerr. 2004. Role of interferons in the treatment of severe acute respiratory syndrome. *Expert Opin. Biol. Ther.* 4: 827–836.
20. Kawai, T., and S. Akira. 2007. Antiviral signaling through pattern recognition receptors. *J. Biochem.* 141: 137–145.
21. Ren, J., Q. Wang, D. Kolli, D. J. Prusak, C. T. Tseng, Z. J. Chen, K. Li, T. G. Wood, and X. Bao. 2012. Human metapneumovirus M2-2 protein inhibits innate cellular signaling by targeting MAVS. *J. Virol.* 86: 13049–13061.
22. Wang, B., X. Xi, X. Lei, X. Zhang, S. Cui, J. Wang, Q. Jin, and Z. Zhao. 2013. Enterovirus 71 protease 2Apro targets MAVS to inhibit anti-viral type I interferon responses. *PLoS Pathog.* 9: e1003231.
23. Horner, S. M., H. M. Liu, H. S. Park, J. Briley, and M. Gale, Jr. 2011. Mitochondrial-associated endoplasmic reticulum membranes (MAM) form innate immune synapses and are targeted by hepatitis C virus. *Proc. Natl. Acad. Sci. USA* 108: 14590–14595.
24. Li, X. D., L. Sun, R. B. Seth, G. Pineda, and Z. J. Chen. 2005. Hepatitis C virus protease NS3/4A cleaves mitochondrial antiviral signaling protein off the mitochondria to evade innate immunity. *Proc. Natl. Acad. Sci. USA* 102: 17717–17722.
25. Wei, C., C. Ni, T. Song, Y. Liu, X. Yang, Z. Zheng, Y. Jia, Y. Yuan, K. Guan, Y. Xu, et al. 2010. The hepatitis B virus X protein disrupts innate immunity by downregulating mitochondrial antiviral signaling protein. *J. Immunol.* 185: 1158–1168.
26. Goswami, R., T. Majumdar, J. Dhar, S. Chattopadhyay, S. K. Bandyopadhyay, V. Verbovetskaya, G. C. Sen, and S. Barik. 2013. Viral degradasome hijacks mitochondria to suppress innate immunity. *Cell Res.* 23: 1025–1042.
27. You, F., H. Sun, X. Zhou, W. Sun, S. Liang, Z. Zhai, and Z. Jiang. 2009. PCBP2 mediates degradation of the adaptor MAVS via the HECT ubiquitin ligase AIP4. *Nat. Immunol.* 10: 1300–1308.
28. Shi, C. S., and J. H. Kehrl. 2010. TRAF6 and A20 regulate lysine 63-linked ubiquitination of Beclin-1 to control TLR4-induced autophagy. *Sci. Signal.* 3: ra42.
29. Gu, J., E. Gong, B. Zhang, J. Zheng, Z. Gao, Y. Zhong, W. Zou, J. Zhan, S. Wang, Z. Xie, et al. 2005. Multiple organ infection and the pathogenesis of SARS. *J. Exp. Med.* 202: 415–424.
30. Farcas, G. A., S. M. Poutanen, T. Mazzulli, B. M. Willey, J. Butany, S. L. Asa, P. Faure, P. Akhavan, D. E. Low, and K. C. Kain. 2005. Fatal severe acute respiratory syndrome is associated with multiorgan involvement by coronavirus. *J. Infect. Dis.* 191: 193–197.
31. Otera, H., N. Ishihara, and K. Mihara. 2013. New insights into the function and regulation of mitochondrial fission. *Biochim. Biophys. Acta* 1833: 1256–1268.
32. Jacobs, J. L., and C. B. Coyne. 2013. Mechanisms of MAVS regulation at the mitochondrial membrane. *J. Mol. Biol.* 425: 5009–5019.
33. Seth, R. B., L. Sun, C. K. Ea, and Z. J. Chen. 2005. Identification and characterization of MAVS, a mitochondrial antiviral signaling protein that activates NF-kappaB and IRF 3. *Cell* 122: 669–682.
34. Nakamura, N., and S. Hirose. 2008. Regulation of mitochondrial morphology by USP30, a deubiquitinating enzyme present in the mitochondrial outer membrane. *Mol. Biol. Cell* 19: 1903–1911.
35. Shi, C. S., K. Shenderov, N. N. Huang, J. Kabat, M. Abu-Asab, K. A. Fitzgerald, A. Sher, and J. H. Kehrl. 2012. Activation of autophagy by inflammatory signals limits IL-1β production by targeting ubiquitinated inflammasomes for destruction. *Nat. Immunol.* 13: 255–263.
36. Maier, H. J., and P. Britton. 2012. Involvement of autophagy in coronavirus replication. *Viruses* 4: 3440–3451.
37. Jounai, N., F. Takeshita, K. Kobiyama, A. Sawano, A. Miyawaki, K. Q. Xin, K. J. Ishii, T. Kawai, S. Akira, K. Suzuki, and K. Okuda. 2007. The Atg5 Atg12 conjugate associates with innate antiviral immune responses. *Proc. Natl. Acad. Sci. USA* 104: 14050–14055.
38. Castanier, C., D. Garcin, A. Vazquez, and D. Arnoult. 2010. Mitochondrial dynamics regulate the RIG-I-like receptor antiviral pathway. *EMBO Rep.* 11: 133–138.
39. Kim, S. J., G. H. Syed, and A. Siddiqui. 2013. Hepatitis C virus induces the mitochondrial translocation of Parkin and subsequent mitophagy. *PLoS Pathog.* 9: e1003285.
40. Rambold, A. S., B. Kostelecky, N. Elia, and J. Lippincott-Schwartz. 2011. Tubular network formation protects mitochondria from autophagosomal degradation during nutrient starvation. *Proc. Natl. Acad. Sci. USA* 108: 10190–10195.
41. Gomes, L. C., G. Di Benedetto, and L. Scorrano. 2011. During autophagy mitochondria elongate, are spared from degradation and sustain cell viability. *Nat. Cell Biol.* 13: 589–598.
42. Wang, H., P. Song, L. Du, W. Tian, W. Yue, M. Liu, D. Li, B. Wang, Y. Zhu, C. Cao, et al. 2011. Parkin ubiquitinates Drp1 for proteasome-dependent degradation: implication of dysregulated mitochondrial dynamics in Parkinson disease. *J. Biol. Chem.* 286: 11649–11658.
43. Purnell, P. R., and H. S. Fox. 2013. Autophagy-mediated turnover of dynamin-related protein 1. *BMC Neurosci.* 14: 86.
44. Youle, R. J., and A. M. van der Bliek. 2012. Mitochondrial fission, fusion, and stress. *Science* 337: 1062–1065.
45. Nakhaei, P., T. Mesplede, M. Solis, Q. Sun, T. Zhao, L. Yang, T. H. Chuang, C. F. Ware, R. Lin, and J. Hiscott. 2009. The E3 ubiquitin ligase Triad3A negatively regulates the RIG-I/MAVS signaling pathway by targeting TRAF3 for degradation. *PLoS Pathog.* 5: e1000650.
46. Jin, R., W. Zhu, S. Cao, R. Chen, H. Jin, Y. Liu, S. Wang, W. Wang, and G. Xiao. 2013. Japanese encephalitis virus activates autophagy as a viral immune evasion strategy. *PLoS One* 8: e52909.
47. Tal, M. C., M. Sasai, H. K. Lee, B. Yordy, G. S. Shadel, and A. Iwasaki. 2009. Absence of autophagy results in reactive oxygen species-dependent amplification of RLR signaling. *Proc. Natl. Acad. Sci. USA* 106: 2770–2775.
48. Subramanian, N., K. Natarajan, M. R. Clatworthy, Z. Wang, and R. N. Germain. 2013. The adaptor MAVS promotes NLRP3 mitochondrial localization and inflammasome activation. *Cell* 153: 348–361.